Assessing the impact of end-member selection on the accuracy of satellite-based spatial variability models for actual evapotranspiration estimation

Di Long[1,2] and Vijay P. Singh[2,3]

[1] This study examines the impact of end-member (i.e., hot and cold extremes) selection on the performance and mechanisms of error propagation in satellite-based spatial variability models for estimating actual evapotranspiration, using the triangle, surface energy balance algorithm for land (SEBAL), and mapping evapotranspiration with high resolution and internalized calibration (METRIC) models. These models were applied to the soil moisture-atmosphere coupling experiment site in central Iowa on two Landsat Thematic Mapper/Enhanced Thematic Mapper Plus acquisition dates in 2002. Evaporative fraction (EF, defined as the ratio of latent heat flux to availability energy) estimates from the three models at field and watershed scales were examined using varying end-members. Results show that the end-members fundamentally determine the magnitudes of EF retrievals at both field and watershed scales. The hot and cold extremes exercise a similar impact on the discrepancy between the EF estimates and the ground-based measurements, i.e., given a hot (cold) extreme, the EF estimates tend to increase with increasing temperature of cold (hot) extreme, and decrease with decreasing temperature of cold (hot) extreme. The coefficient of determination between the EF estimates and the ground-based measurements depends principally on the capability of remotely sensed surface temperature (T_s) to capture EF (i.e., depending on the correlation between T_s and EF measurements), being slightly influenced by the end-members. Varying the end-members does not substantially affect the standard deviation and skewness of the EF frequency distributions from the same model at the watershed scale. However, different models generate markedly different EF frequency distributions due to differing model physics, especially the limiting edges of EF defined in the remotely sensed vegetation fraction (f_c) and T_s space. In general, the end-members cannot be properly determined because (1) they do not necessarily exist within a scene, varying with the spatial extent, resolution, and quality of satellite images being used and/or (2) different operators can select different end-members. Furthermore, the limiting edge of EF = 0 in the f_c-T_s space varies with the model, with SEBAL-type models having inherently an increasing curvilinear limiting edge of EF = 0 with f_c. The spatial variability models therefore require careful calibration in order to deduce reasonable EF-limiting edges and then confine the magnitudes of EF estimates.

[1]Bureau of Economic Geology, Jackson School of Geosciences, The University of Texas at Austin, Austin, Texas, USA.
[2]Department of Biological & Agricultural Engineering, Texas A&M University, College Station, Texas, USA.
[3]Department of Civil & Environmental Engineering, Texas A&M University, College Station, Texas, USA.

Corresponding author: Di Long, Bureau of Economic Geology, Jackson School of Geosciences, The University of Texas at Austin, Austin, TX 78758, USA. (di.long@beg.utexas.edu)

1. Introduction

[2] Actual evapotranspiration (ET_a), comprising vegetation transpiration, surface evaporation, and interception from the vegetative surface, plays a key role in the exchange of water and heat between the land surface and the lower atmosphere. An accurate understanding of the magnitude and distribution of ET_a on the Earth's surface is of importance to many disciplines, e.g., hydrology, agriculture, ecosystem, meteorology, and forestry, and to many related applications, e.g., water resources allocation, irrigation scheduling, crop yield forecasting, weather prediction, drought monitoring, and vulnerability of forests to fire [*Anderson et al.*, 2007; *Bastiaanssen et al.*, 2005; *Long*

and Singh, 2010; *Mackay et al.*, 2007; *McVicar and Jupp*, 1998; *Norman et al.*, 2003; *Verstraeten et al.*, 2008]. Over the last three decades, satellite remote sensing has provided an unprecedented opportunity for capturing the variability in ET_a across a variety of spatial and temporal scales that are not attainable by conventional techniques (e.g., weighing lysimeter, energy balance Bowen ratio (EBBR), and eddy covariance (EC) systems). There are a wide variety of models for ET_a estimation developed by incorporating remotely sensed land surface temperature (T_s) and other critical variables, e.g., albedo (α) and fractional vegetation cover (f_c).

[3] The models, classified as the "spatial variability models" by *Kalma et al.* [2008], are unique in interpreting the contextual relationship between the normalized difference vegetation index (NDVI) or f_c and T_s [e.g., *Batra et al.*, 2006; *Carlson et al.*, 1995a; *Gillies et al.*, 1997; *Jiang and Islam*, 2001; *Price*, 1990], or between α and T_s [e.g., *Roerink et al.*, 2000; *Verstraeten et al.*, 2005] to deduce the evaporative fraction (EF, defined as the ratio of latent heat flux (LE) to available energy (A)) and ET_a. In addition, the surface energy balance algorithm for land (SEBAL) [*Bastiaanssen et al.*, 1998] and a variant, the mapping ET with high resolution and internalized calibration (METRIC) [*Allen et al.*, 2007], pertain to the spatial variability model, as they incorporate the spatial variability in T_s and two constant end-members for a specific scene of image [*Bastiaanssen et al.*, 2002], termed the "hot pixel" and the "cold pixel," to deduce sensible heat (H) and LE by quasi-linear interpolation of extremes.

[4] Several studies have evaluated a range of remote sensing-based ET_a models, which provide insights into the performance of these models under varying soil moisture, environmental, and climatic conditions. *French et al.* [2005a] examined the utility of the two-source energy balance model (TSEB) [*Norman et al.*, 1995] and SEBAL at the soil moisture-atmosphere coupling experiment (SMACEX) site characterized primarily by rainfed corn and soybean in central Iowa in 2002. A bias of ~ -80 W m^{-2} for LE estimates from SEBAL [*French et al.*, 2005b] was attributable to the inability to fully distinguish wet and dry extremes at the study site. *Timmermans et al.* [2007] further examined the utility of TSEB and SEBAL over a subhumid grassland (Southern Great Plains '97) and a subarid rangeland (Monsoon '90) by performing a sensitivity analysis of the two models and comparing their H estimates over different land cover types, confirming that TSEB and SEBAL tend to be most sensitive to T_s, and SEBAL may not be applicable over sparsely vegetated areas. An intercomparison of SEBAL, surface energy balance system (SEBS) [*Su*, 2002], and TSEB was performed, and ET_a estimates from these models were compared with the counterparts from the soil and water assessment tool (SWAT) over a watershed (1850 km^2) in the Chao River basin in North China [*Gao and Long*, 2008]. In general, there was consistency in lumped ET_a estimates from these remote sensing-based models, whereas large differences in the frequency distributions of ET_a were observed. *Gonzalez-Dugo et al.* [2009] compared METRIC, TSEB, and another empirical one-source model at the SMACEX site, showing slightly higher accuracy of ET_a retrievals from the three models than other studies due to the use of measured net radiation (R_n) and soil heat flux (G). *Choi et al.*

[2009] extended their study on a trapezoid NDVI-T_s model, METRIC, and TSEB by comparing output of these models and found significant discrepancies in the spatial distributions of H and LE estimates between different models. Table 1 lists published studies regarding the evaluation of triangle, SEBAL, and METRIC models.

[5] In general, these published studies compared in detail flux estimates with ground-based measurements in terms of root-mean-square difference (RMSD) and bias that describe the magnitude of model-measurement discrepancies. Input variables, applicability of models under a certain environment, sensitive variables, and the distinction between the one-source and the two-source models have been fully discussed [e.g., *French et al.*, 2005a; *Timmermans et al.*, 2007]. However, how the end-member selection compounded by subjectivity impacts the LE estimates, and whether there is a common mechanism for error propagation remain unclear and warrant further investigation. Model intercomparison has suggested notable differences in flux estimates from varying models over an entire modeling domain or a specific land cover type, though in some cases, the one-source and two-source models produced comparable discrepancies with respect to ground-based measurements [e.g., *Choi et al.*, 2009; *French et al.*, 2005a; *Timmermans et al.*, 2007]. Few studies investigated error propagation in terms of model physics and reported the coefficient of determination (R^2). Exploring the fundamental reasons for differences in LE estimates over a modeling domain and examining detailed mechanisms of error propagation could be of great value for a greater understanding of the deficiencies in model physics and improvements to a range of remote sensing-based ET_a approaches.

[6] The objectives of this study, therefore, were to (1) examine how the end-members of the triangle model, SEBAL, and METRIC impact the resulting EF retrievals at the field scale; (2) examine how the end-members impact the frequency distributions of the EF estimates at the watershed scale; (3) examine if the limiting edges of EF within the f_c-T_s space explicitly or implicitly involved in the models can depict the reality; and (4) discuss the common mechanisms of error propagation and potential ways to resolve uncertainties in the spatial variability models.

2. Background Theory

[7] In general, all spatial variability models are based on the equation of energy balance on the Earth's surface:

$$R_n - G = A = H + \text{LE}, \qquad (1)$$

where R_n is the net radiation (W m^{-2}); G is the soil heat flux (W m^{-2}); A is the available energy (W m^{-2}); H is the sensible heat flux (W m^{-2}); and LE is the latent heat flux (W m^{-2}). R_n can be expressed as

$$R_n = (1 - \alpha)S_d + \varepsilon\varepsilon_a\sigma_c T_a^4 - \varepsilon\sigma_c T_s^4, \qquad (2)$$

where S_d is the downwelling shortwave radiation (W m^{-2}); ε is the surface emissivity (dimensionless); ε_a is the atmospheric emissivity (dimensionless); σ_c is the Stefan-Boltzmann constant (5.67×10^{-8} W m^{-2} K^{-4}); and T_a is the air temperature (K).

Table 1. Studies on Evaluation of Three Spatial Variability Models, Including Triangle, SEBAL, and METRIC Models[a]

Model	Literature	Name of Experiment/Study Site, Area, Climate, and Landscape Properties	DOY (Soil Moisture Condition), Sensor Type, and Number of End-Member Pair for Each Scene	Ground-Based Measurement, Energy Closure Approach, and Number of Total Measurements	Accuracy of EF or LE (W m^{-2})
Triangle	Batra et al. [2006]	Southern Great Plains (SGP), ~200,000 km^2, from humid in the east to semiarid in the west, mixed farming, interrupted forest, tall and short grass	115, 163, 190, 229, 276, and 287 in 2001; 91, 99, and 287 in 2002; 82, 90, 91, 262, 285, and 295 in 2003; 15 MODIS, 12 NOAA 14, and 6 NOAA 14; 1	EBBR stations, BR, 60 for MODIS and NOAA16, 21 for NOAA 14	Bias: -29 W m^{-2} for MODIS, 12 W m^{-2} for NOAA16 and -28 W m^{-2} for NOAA14; RMSE: 53 W m^{-2} for MODIS, 51 W m^{-2} for NOAA16, and 55 W m^{-2} for NOAA14; R^2: 0.84 for MODIS, 0.79 for NOAA16, and 0.77 for NOAA14
	Jiang et al. [2009]	Sothern Florida, 124,000 km^2, humid climate, sawgrass, sugar cane, and marsh	Days of clear sky and available ground-based measurements in 1998 and 1999, NOAA14, 1	EBBR stations and lysimeters, BR	Bias: 0.049 RMSE: 0.158
SEBAL	French et al. [2005a, 2005b]	SMACEX, ~670 km^2, humid climate, corn and soybean fields	174 (intermediate) in 2002, ASTER, 1	EC, BR, 8	Bias: -82 W m^{-2}
	Timmermans et al. [2007]	(1) Monsoon '90, ~10 km^2, subhumid, grassland; (2) SGP97, ~45 km^2, semiarid, rangeland	(1) 213 (dry), 216 (wet), 221 (intermediate) in 1990, airborne instruments, 1; (2) 180 (wet) and 183 (intermediate) in 1997, airborne instruments, 1	(1) Variance method, -, 24; (2) EC, BR, 8	MAD: 61 W m^{-2};
	Wang et al. [2009]	Las Cruces in New Mexico, 3600 km^2, pecan and alfalfa, semiarid climate	247 (intermediate) in 2002, ASTER, 1	EC, no correction, 2	MAPD: 23% RMSE: 70 W m^{-2} Relative error: 4.3%–13%
METRIC	Choi et al. [2009]	SMACEX, ~670 km^2, humid climate, corn and soybean fields	174 (intermediate), Landsat TM; 182 (dry), Landsat ETM$^+$ in 2002, 1	EC towers, BR and RE, 18	Bias: 53 W m^{-2} for RE, 19 W m^{-2} for BR; RMSE: 75 W m^{-2} for RE, 55 W m^{-2} for BR
	Gonzalez-Dugo et al. [2009]	SMACEX, ~670 km^2, humid climate, corn and soybean fields	174 (intermediate), Landsat TM; 182 (dry), Landsat ETM$^+$; 189 (wet), Landsat ETM$^+$ in 2002, 3	EC towers, BR and RE, 29	RMSE: 35−44 W m^{-2} for RE, 39−48 W m^{-2} for BR; R^2: 0.85−0.89 for BR, 0.81−0.83 for BR

[a]BR means the Bowen ratio method and RE means the residual energy balance method for energy balance closure for eddy covariance systems. It is noted that biases in Batra et al. [2006] and Choi et al. [2009] were calculated as observed fluxes minus estimated fluxes, instead of other studies as estimated fluxes minus observed fluxes.
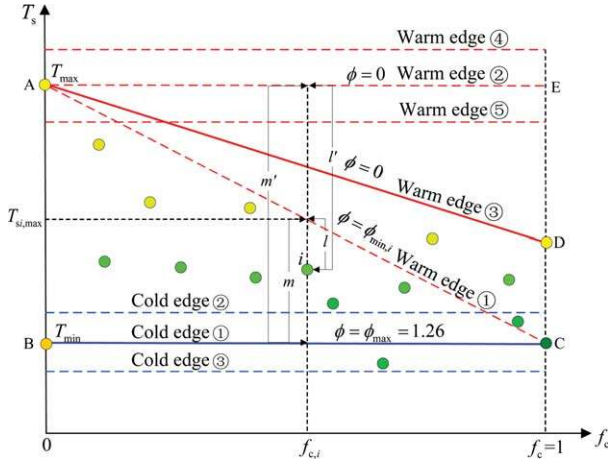
Figure 1. Conceptual scatterplot of remotely sensed f_c and T_s. Colored circles represent surfaces/pixels with varying f_c and T_s. Green color in dots represents relatively high soil surface water content, and yellow color represents relatively low soil surface water content in terms of the concept of soil surface water content isopleths [*Carlson*, 2007; *Carlson et al.*, 1995b]. Trapezoid ABCD represents a trapezoidal framework of the f_c-T_s space [e.g., *Long and Singh*, 2012a; *Moran et al.*, 1994], triangle ABC represents a triangular framework of the f_c-T_s space [e.g., *Jiang and Islam*, 2001; *Sandholt et al.*, 2002], and rectangle ABCE represents a degenerate triangular framework of the f_c-T_s space [e.g., *Batra et al.*, 2006; *Jiang et al.*, 2009]. Warm edges 2, 4, and 5 represent hot extremes possibly selected in triangle, SEBAL, and METRIC models. Cold edges 1–3 represent cold extremes possibly selected in triangle, SEBAL, and METRIC models. Point i represents a pixel within the f_c-T_s space. Distance l represents the difference in T_s between point i and warm edge 1. Distance l' represents the difference in T_s between point i and warm edge 2. Distance m represents the difference in T_s between cold edge 1 and warm edge 1 for point i. Distance m' represents the difference in T_s between cold edge 1 and warm edge 2 for point i.

[8] SEBAL and METRIC compute G as a fraction of R_n as [*Allen et al.*, 2007; *Bastiaanssen*, 2000]

$$G = R_n(T_s - 273.15)(0.0038 + 0.0072\alpha)(1 - 0.98\mathrm{NDVI}^4). \quad (3)$$

[9] Latent heat flux is therefore calculated as the residual of equation (1) when R_n, G, and H are derived in sequence. Triangle models directly deduce EF from the NDVI or f_c-T_s space by interpolating between "warm" and "cold" edges defining nominal boundaries to this distribution of data points (Figure 1). Daily ET_a (mm d^{-1}) is often calculated by using remotely sensed EF, which is assumed to be equivalent to the 24 h average EF to partition daily net radiation as SEBAL and the triangle model do [*Bastiaanssen et al.*, 2002; *Jiang et al.*, 2009; *Long et al.*, 2010]. However, this assumption can result in uncertainties in the ET_a estimates under partial cloudy conditions throughout a day, across areas where nocturnal transpiration is large [*Van Niel et al.*, 2011] and forested areas where rainfall interception and subsequent evaporation from the canopy can be

appreciable [*Schellekens et al.*, 1999]. METRIC computes daily ET_a by using the reference ET fraction at the satellite overpass time, which is assumed equal to the 24 h average ET fraction to partition daily reference ET [*Allen et al.*, 2007]. Comparison based on EF instead of LE or ET_a in this study was intended to isolate the effect of R_n on LE, adopting a straightforward scale to assess the impact of end-members on the output from triangle, SEBAL, and METRIC models.

2.1. Triangle Models

[10] Figure 1 also shows a conceptual representation of triangle models. EF for a pixel i from the triangle model [e.g., *Jiang and Islam*, 2001] is estimated by interpolating parameter ϕ of the cold edge ($\phi = 1.26$, corresponding to cold edge 1 in Figure 1) and the warm edge ($\phi = 1.26\mathrm{NDVI}_i/\mathrm{NDVI}_{max}$ or $\phi = 1.26 f_{c,i}/f_{c,max}$, corresponding to warm edge 1 in Figure 1) based on the ratio of the T_s difference between warm edge 1 and pixel i (l in Figure 1) to the T_s difference between warm edge 1 and cold edge 1 (m in Figure 1). Later, the warm edge of the triangle model was simplified as a constant hot extreme (point A and warm edge 2 in Figure 1) [*Batra et al.*, 2006; *Jiang et al.*, 2009]. The ϕ value for the horizontal warm edge is taken to be zero, and the ϕ value for a pixel i is interpolated based on the ratio of the T_s difference between warm edge 2 and pixel i (l' in Figure 1) to the T_s difference between warm edge 2 and cold edge 1 (m' in Figure 1). EF from the triangle model can be written as [*Batra et al.*, 2006; *Choi et al.*, 2009; *Jiang et al.*, 2009]

$$\mathrm{EF} = \phi_{max}\frac{T_{max} - T_s}{T_{max} - T_{min}} \cdot \frac{\Delta}{\Delta + \gamma}, \quad (4)$$

where ϕ_{max} is equal to 1.26; T_{max} and T_{min} are the temperatures (K) of the hot extreme and cold extremes throughout a scene; Δ is the slope of saturated vapor pressure at T_a (kPa °C^{-1}); and γ is the psychometric constant (kPa °C^{-1}). The quantity $\Delta/(\Delta+\gamma)$ remains fairly invariant under generally homogenous meteorological fields (i.e., T_a, vapor pressure e_a, and wind velocity u). It is apparent from equation (4) that variation in EF with T_s follows an inverse linear relation; T_{max} and T_{min} play a key role in determining EF.

2.2. SEBAL

[11] SEBAL calculates H by assuming a linear relationship between ΔT and T_s across an entire image where ΔT (K) is the difference between the aerodynamic temperature and T_a [*Bastiaanssen et al.*, 1998, 2005]. This assumption obviates the specification of roughness length for heat transfer parameterized in the one-source models that cannot be assessed on the basis of generic rules in heterogeneous landscapes [*Bastiaanssen et al.*, 2005; *Carlson et al.*, 1995c]. Coefficients of the linear relationship are determined by a hot extreme and a cold extreme selected by the operator from the satellite image. For the hot extreme, LE is taken to be zero; thus, H for the hot extreme is equal to its available energy. For the cold extreme, H is taken to be zero and LE for the cold extreme is equal to the available energy. Sensible heat flux from SEBAL is calculated as

$$H = \rho c_p \frac{\Delta T}{r_{ah}} = \rho c_p \frac{aT_s + b}{r_{ah}}, \tag{5}$$

where ρ is the air density (kg m^{-3}); c_p is the specific heat of air at constant pressure (J kg^{-1} K^{-1}); r_{ah} is the aerodynamic resistance (s m^{-1}) [*Long and Singh*, 2012b]; and a (dimensionless) and b (K) are the coefficients of the assumed linear relationship between T_s and ΔT derived by the two extremes:

$$a = \frac{r_{ah,hot}}{\rho_{hot} c_p} \cdot \frac{A_{hot}}{T_{max} - T_{min}}, \tag{6}$$

$$b = -aT_{min}, \tag{7}$$

where subscript hot denotes variables for the hot extreme. *Long et al.* [2011] showed that T_{max}, T_{min}, and A_{hot} are the most sensitive variables associated with end-members in SEBAL, and the hot extreme plays a more prominent role than does the cold extreme. Latent heat flux can be eventually obtained by equation (1) after R_n, G, and H are calculated.

[12] From the perspective of the f_c-T_s space, the two extremes in SEBAL bound two limiting edges of EF [*Long and Singh*, 2012b]. Sensible heat flux and EF for each f_c class can be calculated using the following equations:

$$H_i = \rho c_p \frac{\Delta T}{r_{ah,i}} = \rho c_p \frac{aT_s + b}{r_{ah,i}}, \tag{8}$$

$$EF_i = \frac{A_i - H_i}{A_i} = 1 - \frac{H_i}{A_i}, \tag{9}$$

where subscript i denotes variables in the f_c class i.

2.3. METRIC

[13] METRIC inherits the key assumption of linear correlation of T_s with ΔT from SEBAL and interpolation of H for all pixels in an image, except the end-members in terms of coefficients a and b [*Allen et al.*, 2007]. It differs from SEBAL in a slight modification of the energy balance for the two extremes, considering conditions deviating somewhat from the reality. This means that METRIC does not strictly require zero LE = 0 at the hot extreme where a soil water balance model [*Allen et al.*, 1998] is used to infer residual soil evaporation for the hot extreme. The cold extreme is tied to measurements of reference ET made at a ground station somewhere within the modeling domain. The use of reference ET, which is sometimes larger than available energy for the cold extreme, partly accounts for the impact of advection on the energy balance for the cold extreme [*Choi et al.*, 2009]. However, the modification does not substantially alter the model physics of SEBAL, which may make METRIC exhibit similar performance and mechanisms of error propagation as does SEBAL. Coefficients a and b of METRIC are incorrectly expressed in *Allen et al.* [2007]. They are, in fact, in the forms below (note that coefficients a and b in this study correspond to b and a in equation (29) in *Allen et al.* [2007]):

$$a = \frac{dT_{hot} - dT_{cold}}{T_{max} - T_{min}}, \tag{10}$$

$$b = dT_{hot} - aT_{max}, \tag{11}$$

$$dT_{hot} = \frac{(A_{hot} - LE_{hot})r_{ah,hot}}{\rho_{hot} c_p}, \tag{12}$$

$$dT_{cold} = \frac{(A_{cold} - LE_{cold})r_{ah,cold}}{\rho_{cold} c_p}, \tag{13}$$

where subscript cold denotes variables for the cold pixel. It is apparent that in SEBAL LE$_{hot}$ in equation (12) is zero, and dT_{cold} becomes zero due to LE$_{cold}$ = A_{cold}. In METRIC, LE$_{cold}$ is inferred by the American Society of Civil Engineers (ASCE)-standardized Penman-Monteith reference ET multiplied by a reference ET fraction (ET$_r$F) of 1.05 [*Allen et al.*, 2007], and LE$_{hot}$ is calculated by the reference ET multiplied by ET$_r$F for the hot extreme, which is estimated by a soil water balance model [*Allen et al.*, 1998].

[14] Note that all the three spatial variability models require the selection of end-members from satellite images by the operator. Efforts on automating the selection of end-members have been made [e.g., *McVicar and Jupp*, 1999, 2002] and are still ongoing for SEBAL and METRIC [*Allen et al.*, 2007; *Choi et al.*, 2009], which would reduce subjectivity. Characteristic variables of the end-members, e.g., T_{max}, and T_{min}, are subsequently derived and constitute input of equations (4) and (6)–(13). It is assumed that points A and B in Figure 1 represent the realistic hot and cold extremes that can meet the basic assumptions of these models. There are three possibilities for a hot extreme and a cold extreme to be selected or specified, corresponding to warm edges 2, 4, and 5, and cold edges 1–3 in Figure 1.

3. Materials

3.1. Study Site

[15] The SMACEX campaign was conducted in central Iowa, USA, ranging in latitude between 41.87°N and 42.05°N and in longitude between −93.83°W and −93.39°W (Figure 2) between 15 June (day of year (DOY) 166) through 8 July (DOY 189) in 2002. It provided extensive measurements of soil, vegetation, and meteorological properties and states for a greater understanding of mechanisms of water and heat exchanges with the atmosphere [*Kustas et al.*, 2005]. The field campaign was primarily conducted in the Walnut Creek watershed, just south of Ames in central Iowa. Rainfed corn and soybean fields dominate the Walnut Creek watershed. These crops grew rapidly during the campaign.

[16] The mean annual rainfall of this region is 835 mm/year, which is classified as a humid climate. Precipitation during the campaign occurred a few days prior to 15 June (DOY 166), with a minor rainfall event wetting the soil surface in most areas with either 0–5 mm or 5–10 mm of precipitation on 20 June (DOY 171). This was followed by a drydown period for the Walnut Creek watershed until 4 July (DOY 185) [*Kustas and Anderson*, 2009; *Kustas et al.*, 2005]. The topography is characterized by low relief and poor surface drainage, with a mean elevation of ∼300
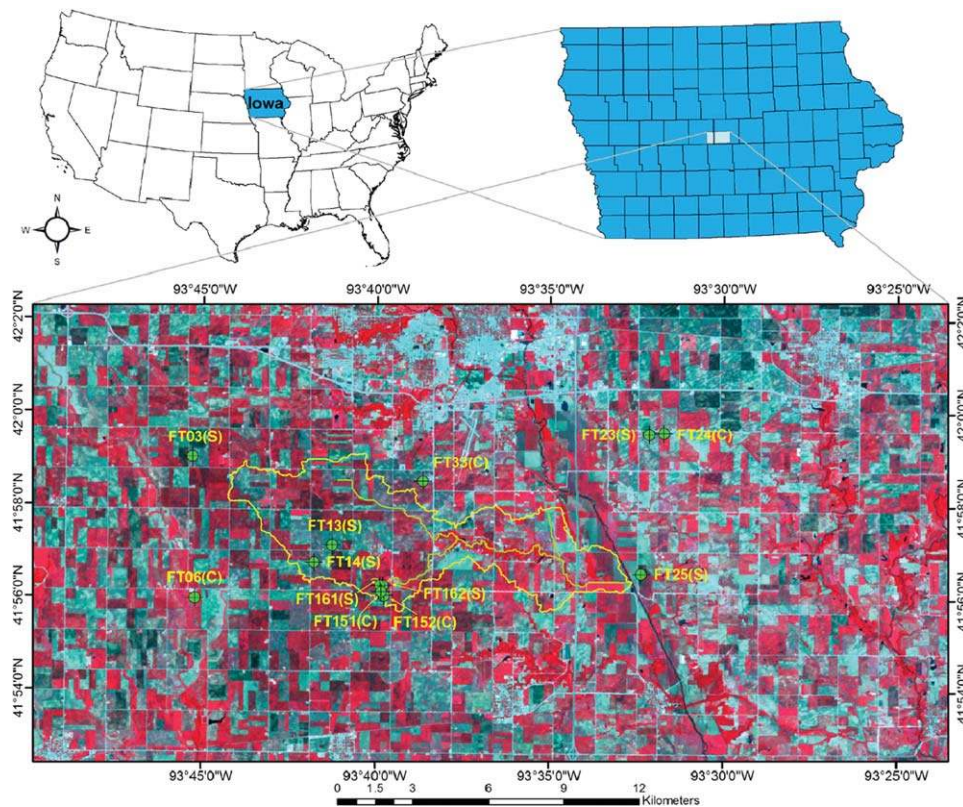
Figure 2. Location and false color composite of Landsat TM imagery acquired on 23 June 2002, of the SMACEX site in Ames, central Iowa, USA. The Walnut Creek watershed is delineated in yellow and the main Walnut Creek and its branch are shown in green. The meteorological-flux (METFLUX) network, comprising 12 field sites, is shown in numbered green circles nested with cross wires. Letter C denotes corn and S denotes soybean for the major crop type at each EC tower.

m. The extensive measurements of surface fluxes in combination with diverse agricultural crops make the SMACEX site an ideal test bed for evaluating a range of remote sensing-based models [e.g., *Anderson et al.*, 2007; *Choi et al.*, 2009].

3.2. Flux Tower Measurements

[17] A network consisting of 12 fully operational meteorological-flux (METFLUX) towers was deployed within or in the vicinity of the Walnut Creek watershed (flux tower (FT) 13, 14, 151, 152, 161, 162 within the watershed; FT03, 06, 23, 24, 25, and 33 outside the watershed), employing EC systems at 12 field sites, in which five sites were corn and seven sites were soybean (Figure 2). These towers were instrumented with a variety of sensors for measuring turbulent fluxes of LE and *H*, as well as radiation components (i.e., incoming and outgoing shortwave and longwave radiation) and soil heat fluxes at 30 min intervals. Additional in situ hydrometeorological observations encompassed 10 min averaged T_a, relative humidity, and wind speed and direction. Air temperature and relative humidity were measured at heights ranging between 1.16 m and 2.66 m for different EC towers but remained unchanged during the campaign. Wind velocity was measured at heights ranging between 1.83 m and 5.03 m for differing EC towers during the campaign, five of which in corn fields were elevated by 1–2 m between DOY 179 and DOY 181 to accommodate growth in the corn. Observed

EF calculated by observed LE over the sum of observed LE and *H*, i.e., preserving the Bowen ratio, at these EC towers for two image acquisition dates [e.g, *Anderson et al.*, 2005, 2007; *French et al.*, 2005b] was used to evaluate the three spatial variability models. If the energy balance closure is achieved by the residual method, i.e., ground-based LE derived from observed R_n-*G*-*H*, storage corrections to soil heat flux measurements should be performed. Table 2 contains three statistical metrics quantifying the discrepancies between measurements and estimates. EF estimates from the three spatial variability models were averaged over the estimated upwind source-area/footprint for each flux tower using the approach proposed by *Li et al.* [2008]. Details of these sensors and processing of measurements can be found in *Kustas et al.* [2005] and *Prueger et al.* [2005].

3.3. Remote Sensing Data Sources and Variable Derivation

[18] During SMACEX, three cloud-free scenes of Landsat Thematic Mapper (TM)/Enhanced Thematic Mapper Plus (ETM+) imagery were acquired, two of which were used in this study. One scene of Landsat TM was acquired at 10:20 A.M. (local time) on DOY 174 (23 June 2002) spanning vegetated canopy cover from 50% to 75%. The other scene of Landsat ETM+ was acquired at 10:42 A.M. (local time) on DOY 182 (1 July 2002) spanning vegetated canopy cover from 75% to 90%. Land surface temperature was retrieved from the thermal band of the Landsat images

Table 2. Description of Statistics Used in This Study[a]

Statistical Variables	Description	Equation
μ	Sample mean	$\frac{1}{n}\sum_{i=1}^{n} P_i$
σ	Standard deviation	$\left[\dfrac{\sum_{i=1}^{n}(P_i-\mu)^2}{n-1}\right]^{1/2}$
γ	Skewness	$\dfrac{\frac{1}{n}\sum_{i=1}^{n}(P_i-\mu)^3}{\left[\frac{1}{n}\sum_{i=1}^{n}(P_i-\mu)^2\right]^{3/2}}$
RMSD	Root-mean-square difference	$\left[\frac{1}{n}\sum_{i=1}^{n}(P_i-Q_i)^2\right]^{1/2}$
MAPD	Mean absolute percentage difference	$100\times\frac{1}{n}\sum_{i=1}^{n}\left|\frac{P_i-Q_i}{Q_i}\right|$
Bias	Bias	$\frac{1}{n}\sum_{i=1}^{n}(P_i-O_i)$

[a]In equations, P_i represents a sample of model simulations and O_i represents a sample of ground-based observations.

using parameters specifically for the SMACEX site [*Li et al.*, 2004], with uncertainties within ~1°C for the Landsat ETM[+] image and ~1.5°C for the Landsat TM image. Albedo was retrieved from the visible, near-infrared, and shortwave infrared bands of the Landsat images using *Allen et al.* [2007]'s algorithm. Spatial mean of T_a across all EC towers at the satellite overpass time was 29.6°C and 29.4°C for DOY 174 and DOY 182, respectively, with DOY 174 showing a smaller standard deviation of 0.34°C than DOY 182 with a standard deviation of 0.42°C. Information on antecedent precipitation, f_c, and meteorological conditions suggests that DOY 174 had a more homogenous surface moisture and meteorological condition than DOY 182.

4. Methods

4.1. Selection of End-Members

[19] A brief review of the three spatial variability models in section 2 shows that T_{max} and T_{min} bound EF within a scene. EF for the remaining pixels is linearly or quasi-linearly interpolated by the two extremes [*Choi et al.*, 2009; *Long and Singh*, 2012b], and hence they play a critical role in determining the resultant EF or LE across a scene. To test this hypothesis, EF was simulated by the three spatial variability models in combination with differing end-members. Three operators having knowledge of remote sensing and the spatial variability models selected end-members against the scatterplot of the f_c-T_s space (Figure 3) and land cover map of the SMACEX site, with three hot extremes and three cold extremes identified for each day. The three hot and three cold pixels resulted in nine (3×3) combinations of end-members for subsequent calculation of EF (Table 3).

[20] The hot pixels for DOY 174 were selected north, west, and south of the study domain, respectively (Figure 4a), which were indentified to be a bare surface (hot pixel 1) and late plantings of a soybean crop (hot pixels 2 and 3).

The cold pixels were selected from the corn fields with f_c ranging from 0.84 to 0.9 in the southeast (cold pixel 1) and west (cold pixels 2 and 3). For DOY 182, the hot extremes were selected from the bare surfaces with low f_c, ranging from 0.13 to 0.14 in the north of the study domain (Figure 4b). The cold extremes were concentrated in the corn fields, with f_c ranging from 0.87 to 0.92 in the east. It is noted that differences in T_{max} or T_{min} were within 1°C for DOY 174 but within 3°C for DOY 182 (Table 3). This is attributed to the combined effect of higher spatial resolution of T_s (60 m) and soil moisture variability for DOY 182 (standard deviation of T_s: 3.3°C) than DOY 174 (the spatial resolution of T_s: 120 m; the standard deviation of T_s: 2.8°C). A larger contrast in soil surface water content and, consequently, T_s would likely result in larger differences in the selected end-members.

[21] Furthermore, there is no certain pattern for the distribution of end-members at the SMACEX site, which could be due in part to the large variability in convective precipitation and rapid change in soil moisture in summer. An additional hot extreme was deduced by extrapolating the warm edge of the f_c-T_s space to intersect with $f_c = 0$
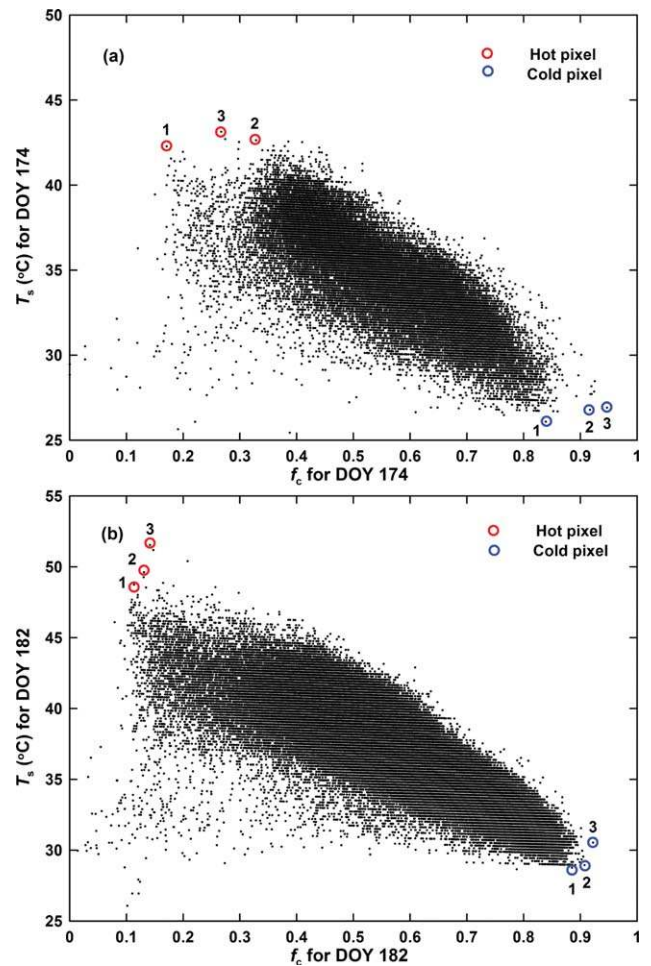

Figure 3. Scatterplots of f_c and T_s for the SMACEX site in central Iowa, USA, on (a) DOY 174 and (b) DOY 182 in 2002. Numbered red circles (1–3) represent hot extremes, and numbered blue circles (1–3) represent cold extremes selected by different operators.

Table 3. Hot and Cold Extremes With Their Characteristic Variables at the Soil Moisture Atmosphere Coupling Experiment (SMA-CEX) Site for DOY 174 and DOY 182 in 2002[a]

| Case (Hot, Cold) | FT | | | | T_{max} (°C) | | A_{hot} (W m^{-2}) | | $f_{c,hot}$ | | T_{min} (°C) | | A_{cold} (W m^{-2}) | | $f_{c,cold}$ | |
| | 174 | | 182 | | | | | | | | | | | | | |
174 and 182	Hot	Cold	Hot	Cold	174	182	174	182	174	182	174	182	174	182	174	182
1 (1, 1)	33	25	33	24	42.3	48.7	481.7	442.5	0.17	0.13	26.1	28.8	593.0	610.9	0.84	0.87
2 (2, 1)	06	25	33	24	42.6	49.6	478.3	440.9	0.33	0.13	26.1	28.8	593.0	610.9	0.84	0.87
3 (3, 1)	25	25	33	24	43.1	51.5	467.0	442.5	0.27	0.14	26.1	28.8	593.0	610.9	0.84	0.87
4 (1, 2)	33	06	33	24	42.3	48.7	481.7	442.5	0.17	0.13	26.8	29.0	588.1	638.1	0.92	0.90
5 (2, 2)	06	06	33	24	42.6	49.6	478.3	440.9	0.33	0.13	26.8	29.0	588.1	638.1	0.92	0.90
6 (3, 2)	25	06	33	24	43.1	51.5	467.0	442.5	0.27	0.14	26.8	29.0	588.1	638.1	0.92	0.90
7 (1, 3)	33	06	33	24	42.3	48.7	481.7	442.5	0.17	0.13	26.9	30.5	570.9	550.9	0.94	0.92
8 (2, 3)	06	06	33	24	42.6	49.6	478.3	440.9	0.33	0.13	26.9	30.5	570.9	550.9	0.94	0.92
9 (3, 3)	25	06	33	24	43.1	51.5	467.0	442.5	0.27	0.14	26.9	30.5	570.9	550.9	0.94	0.92

[a]Column 1 shows nine combinations of three hot pixels (numbered 1–3) and three cold pixels (numbered 1–3) for both days, referring to Figure 3 showing these extremes on the scatterplots of f_c and T_s for DOY 174 and DOY 182. FT means IDs of eddy covariance towers for calculating reference ET as input for METRIC.
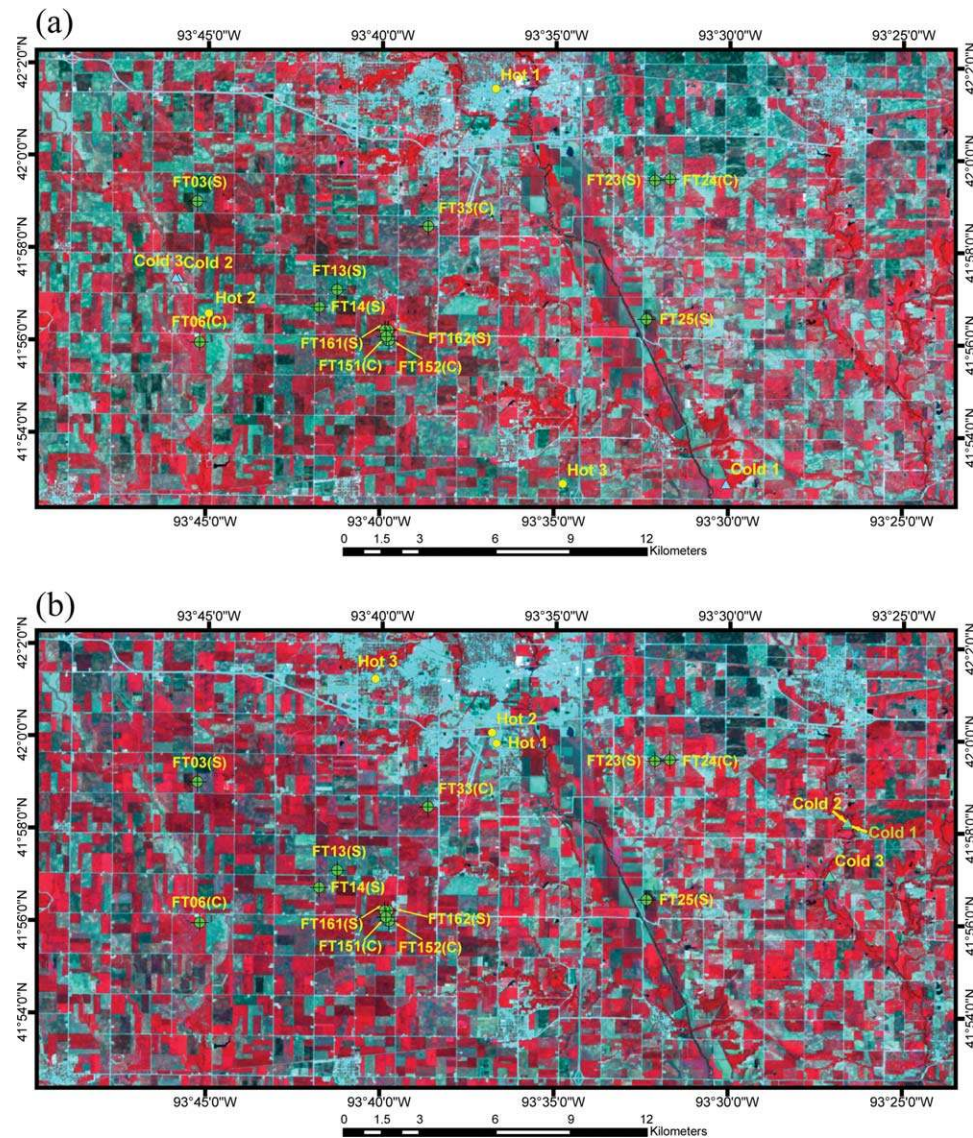
Figure 4. End-members for (a) DOY 174 and (b) DOY 182 at the SMACEX site selected by different operators.

[*Batra et al.*, 2006]. However, the deduced hot extreme in conjunction with the triangle model failed to generate acceptable EF estimates, thereby not being involved in further discussion.

[22] Reference ET values of the selected end-members were calculated using meteorological data from the nearest EC towers as input for METRIC (Figure 4 and Table 3). Typical values of ET_rF for hot pixels vary between 0 and 0.1, and 0.1 could be appropriate during the SMACEX campaign based on *Choi et al.* [2009], though the soil water balance model showed values smaller than 0.1 for the 2 days being tested.

4.2. Theoretical Expression of Limiting Edges of EF for Triangle and SEBAL-Type Models

[23] Definitions of limiting edges of EF are different in the spatial variability models, but these differences and associated potential deficiencies have not yet been systematically investigated. Furthermore, there remains a question: Are the definitions of these limiting edges reasonable? It is apparent from equation (4) that EF for the warm edge of the triangle model (segment AE in Figure 1) is zero ($T_s = T_{max}$); EF for the cold edge is equal to the quantity $1.26\Delta/(\Delta+\gamma)$, which is equal to 1 when $T_a = 31.2°C$ and to 0.93 when $T_a = 25°C$.

[24] It is noted that the limiting edges of EF in SEBAL are not explicitly shown because the interpolation is applied to H rather than EF. It can be derived that EF for the cold edge of SEBAL is equal to 1 in terms of equations (6)–(9) when $T_s = T_{min}$. Here, we derive the limiting edge of $EF = 0$ inherent in SEBAL. Writing the first two terms of the Taylor series of A_i at T_a results in the following:

$$A_i(T_s) = R_n(T_s) - G(T_s) \approx R_n(T_a) + \frac{\partial R_n}{\partial T_s}\Big|_{T_s=T_a}$$
$$(T_s - T_a) - G(T_a) - \frac{\partial G}{\partial T_s}\Big|_{T_s=T_a}(T_s - T_a)$$
$$= [R_n(T_a) - G(T_a)] + (T_s - T_a)\left(\frac{\partial R_n}{\partial T_s}\Big|_{T_s=T_a} - \frac{\partial G}{\partial T_s}\Big|_{T_s=T_a}\right)$$
$$= A_i(T_a) + (T_s - T_a)\Delta',$$
$$(14)$$

$$\frac{\partial R_n}{\partial T_s} = -4\varepsilon\sigma T_s^3, \tag{15}$$

$$\frac{\partial G}{\partial T_s} = (0.0038 + 0.0072\alpha)(1 - 0.98NDVI^4)$$
$$[R_n - 4\varepsilon\sigma T_s^3(T_s - 273.15)], \tag{16}$$

where $A_i(T_a)$ is the net energy for pixels in f_c class i, in which T_s is replaced by T_a and Δ' is the derivative part of the second term of the Taylor series of $A_i(T_s)$.

[25] Let equation (9) be equal to zero. Combining equations (8) and (14)–(16) results in

$$T'_{max} \approx \frac{A_i(T_a) - T_a\Delta' - \rho c_p \frac{b}{r_{ah,i}}}{\rho c_p \frac{a}{r_{ah,i}} - \Delta'}, \tag{17}$$

where T'_{max} is the temperatures of the driest surfaces where EF is equal to 0 for a full range of f_c in SEBAL. Meteoro-

logical fields were generally uniform at the study site [*Long and Singh*, 2012a]. Variation in T'_{max} with f_c is, hence, caused primarily by variation in α in $A_i(T_a)$ and the roughness length for momentum transfer, z_{om}, in $r_{ah,i}$. We suggest that the functional relationship between α and f_c for the limiting edge of $EF = 0$ can be approximated by the upper envelope of the scatterplot of f_c and α [*Long and Singh*, 2012b], because the driest surface tends to have the largest α given an f_c class. The functional relationship between z_{om} and f_c can be constructed using the method of *Tasumi* [2003]. Coefficients a and b are derived from the combination of end-members, which resulted in the highest EF accuracy shown in section 5.1.

5. Results

5.1. EF Estimates at the Field Scale Using Different End-Members

[26] Comparison of ground-based EF measurements and EF estimates from the three models using nine combinations of end-members is displayed in Table 4 and Figure 5. There are five key points to be made from this investigation.

[27] First, differing combinations of end-members can result in largely different magnitudes of the EF estimates at EC towers, showing the mean absolute percentage difference (MAPD) for the triangle model ranging between $\sim$27.1% and 33.8% on DOY 174 and between 9.2% and 13.1% on DOY 182. SEBAL and METRIC show generally smaller discrepancies, with MAPD for SEBAL ranging between 19.3% and 27.7%, and between 7.4% and 12.4%, and MAPD for METRIC ranging between 10.7% and 17.9%, and between 8.3% and 14.7% on the 2 days, respectively. It is also noted that for the three models, the highest and lowest accuracy of the EF estimates occur under two extreme cases, i.e., the greatest/smallest T_s for both end-members. For instance, the triangle model combined with hot pixel 1 and cold pixel 1, both of which are the lowest temperatures in the hot extremes and cold extremes being selected (referring to Table 3 and Figure 3), generated EF with the largest errors in all combinations of end-members. In contrast, the highest accuracy occurred under the combination of hot pixel 3 and cold pixel 3 for both days, which are the highest temperatures in the hot extremes and cold extremes. SEBAL and METRIC also show similar correlation between the retrieval accuracy and the combinations of end-members.

[28] Second, given a cold extreme, the EF estimates from the three models increase with increasing hot extremes and decrease with decreasing hot extremes. Likewise, given a hot extreme, the EF estimates increase with increasing cold extremes and decrease with decreasing cold extremes. This means that the two end-members have a similar function in determining the magnitudes of EF estimates. They both play a key role in determining the overall discrepancy (bias, RMSD, and MAPD) between predictions and measurements. It is important to note that if the two extremes move in the opposite direction, the EF estimates for pixels with moderate T_s values may remain relatively invariant; however, the EF estimates for pixels with T_s values close to the two extremes are changed more

Table 4. Discrepancies Between EF Estimates From Triangle, SEBAL, and METRIC Models and Corresponding Measurements Under Nine Combinations of Selected Extremes on DOY 174 and DOY 182[a]

Model	Cold Pixel	Hot Pixel	Case	DOY 174				DOY 182			
				R^2	RMSD	MAPD	Bias	R^2	RMSD	MAPD	Bias
Triangle	1	1	1	*0.96*	*0.24*	*33.83*	*−0.24*	*0.46*	*0.13*	*13.07*	*−0.09*
		2	2	0.96	0.23	32.55	−0.23	0.46	0.12	11.58	−0.08
		3	3	0.96	0.22	30.50	−0.21	0.46	0.10	8.83	−0.05
	2	1	4	0.96	0.22	30.85	−0.22	0.46	0.12	12.39	−0.08
		2	5	0.96	0.21	29.56	−0.21	0.46	0.11	10.92	−0.07
		3	6	0.96	0.20	27.51	−0.19	0.46	0.09	8.26	−0.05
	3	1	7	0.96	0.22	30.40	−0.21	0.46	0.10	10.03	−0.03
		2	8	0.96	0.21	29.11	−0.20	0.46	0.10	9.46	−0.02
		3	9	*0.96*	*0.19*	*27.07*	*−0.19*	*0.46*	*0.09*	*9.17*	*0.00*
SEBAL	1	1	1	*0.91*	*0.20*	*27.68*	*−0.19*	*0.43*	*0.08*	*7.39*	*−0.01*
		2	2	0.91	0.19	25.96	−0.18	0.43	0.08	7.51	0.00
		3	3	0.90	0.17	22.50	−0.16	0.43	0.08	8.00	0.02
	2	1	4	0.91	0.17	23.07	−0.16	0.43	0.08	7.61	0.00
		2	5	0.91	0.15	19.69	−0.14	0.43	0.08	7.72	0.01
		3	6	0.91	0.15	19.69	−0.14	0.43	0.08	8.32	0.03
	3	1	7	0.91	0.18	24.34	−0.17	0.44	0.09	10.35	0.04
		2	8	0.91	0.17	22.64	−0.16	0.44	0.09	10.97	0.05
		3	9	*0.91*	*0.14*	*19.27*	*−0.13*	*0.44*	*0.10*	*12.37*	*0.07*
METRIC	1	1	1	*0.90*	*0.13*	*17.88*	*−0.13*	*0.43*	*0.08*	*8.25*	*0.03*
		2	2	0.90	0.12	16.41	−0.12	0.43	0.08	8.79	0.04
		3	3	0.90	0.10	13.46	−0.10	0.43	0.09	10.20	0.05
	2	1	4	0.91	0.11	13.96	−0.10	0.43	0.08	8.55	0.03
		2	5	0.91	0.11	13.96	−0.10	0.43	0.08	9.13	0.04
		3	6	0.91	0.09	11.07	−0.08	0.43	0.09	10.70	0.06
	3	1	7	0.91	0.11	15.04	−0.11	0.44	0.10	12.52	0.07
		2	8	0.91	0.10	13.59	−0.10	0.44	0.11	13.36	0.08
		3	9	*0.91*	*0.08*	*10.72*	*−0.08*	*0.44*	*0.12*	*14.74*	*0.09*

[a]Cold pixels 1–3 and hot pixels 1–3 are in increasing order of the magnitude of temperature (referring to Figure 5), respectively. Statistics R^2, RMSD, and MAPD represent the coefficient of determination, root-mean-square difference, and MAPD (Table 2). The values in italics show extreme statistics from the nine cases for each model on each day.

prominently due to the varying extremes. So while end-members involve uncertainties, there is still a possibility that EF estimates from spatial variability models show agreement with ground-based measurements at a handful of flux towers with moderate T_s values [e.g., *Choi et al.*, 2009; *Timmermans et al.*, 2007].

[29] Third, in general, the triangle model underestimates EF, showing negative biases for all combinations of extremes for both days (Table 4). The underestimation may be related to both selected end-members being lower than the realistic ones for the triangle model (corresponding to the combination of warm edge 5 and cold edge 3 in Figure 1). As such, with the selected end-members incrementally moving upward (i.e., increasing T_{max} and T_{min}), errors involved in the EF estimates from the triangle model can be reduced to varying degrees. The same explanation can also be applied to the underestimation of EF from SEBAL and METRIC for DOY 174, with errors generally decreasing with the two end-members being increased. For DOY 182, SEBAL/METRIC overestimates EF by the same amount as the triangle model underestimates. The combination of cold pixel 1 and hot pixel 1 seemed to result in the highest accuracy for both SEBAL and METRIC, with errors generally increasing with the two end-members progressively moving upward.

[30] Fourth, R^2 of different models seems to be essentially of the same order ($R^2 > 0.9$ and ~0.4 for DOY 174 and 182, respectively). Differences in R^2 for different days can be ascribed to varying degrees of correlation of T_s and EF measurements. Linear regression analysis of T_s and ground-based EF measurements shows R^2 of 0.96 and 0.46 for DOY 174 and DOY 182, respectively (Figure 6), which is the same as R^2 for the triangle model, but slightly degraded by SEBAL and METRIC as R^2 of ~0.90 and ~0.44 for DOY 174 and 182, respectively (referring to Table 4). These findings demonstrate that all spatial variability models tested here have no substantially different R^2, which characterizes the ability of predictions to explain variability in measurements. Utility of these models appears to depend largely on the capability of T_s to capture EF. Model mechanisms and end-members play a negligible role in determining R^2 over relatively homogenous agricultural fields. The primary differences in these spatial variability models lie in the definition of limiting edges of EF, which largely determines the magnitude and frequency distributions of the EF estimates to be shown in section 5.2.

[31] Fifth, R^2 remains fairly invariant using varying end-members for the same model, which means that varying end-members does not impact the R^2 of a model but functions in controlling the magnitudes and frequencies of EF estimates. Consistent overestimation or underestimation of EF by a spatial variability model can take place due to an inappropriate selection or specification of end-members or an unrealistic definition of its limiting edges. If ground-based measurements are available, the discrepancies between estimates and measurements can be alleviated by tuning the variables or parameters of end-members. METRIC uses ground-based reference ET and/or the priori knowledge about the crop coefficient to resolve the energy balance equation for the cold extreme, and attempts to infer
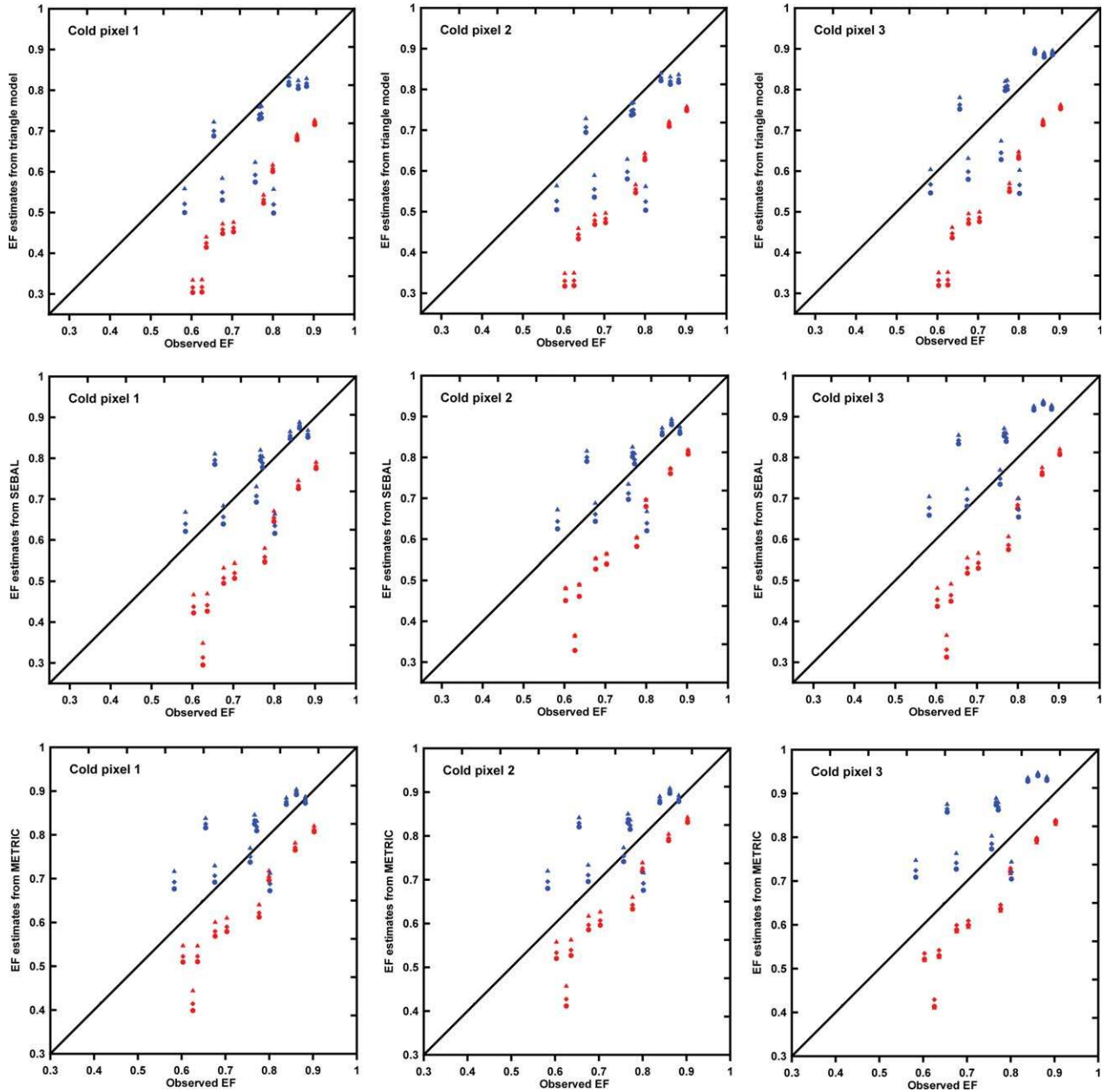
Figure 5. Comparison of flux tower EF measurements and EF estimates from the triangle model, SEBAL, and METRIC for nine combinations of selected extremes on DOY 174 (red symbols) and DOY 182 (blue symbols), respectively. Circles denote the combination of hot pixel 1 and the corresponding cold pixels (1–3) shown in each subplot. Diamonds denote the combination of hot pixel 2 and the corresponding cold pixels (1–3). Triangles denote the combination of hot pixel 3 and the corresponding cold pixels (1–3).

the possible LE for the hot extreme using a soil water balance model. To that end, spatial variability models entail a calibration procedure to constrain the EF magnitudes within a reasonable range, which is intrinsic in the spatial variability models but has not been discussed in the literature to date.

5.2. EF Estimates at the Watershed Scale Using Different End-Members

[32] Frequency distributions of EF estimates from the triangle model and SEBAL across the study domain for DOY 174 are shown in Figures 7 and 8 (those for METRIC for DOY 174 and all models for DOY 182 are provided in the Supporting Information). Statistical metrics of spatial mean, standard deviation, and skewness (Table 2) for these EF frequency distributions for both days are presented in Table 5. Four key points can be implied in the following.

[33] First, the three spatial variability models generated larger EF estimates when the hot or cold extreme moved upward (increasing T_{max} or T_{min}). This characteristic can be demonstrated by cases 1–3, 4–6, and 7–9 with increasing T_{max} and a fixed T_{min} for both days, showing a
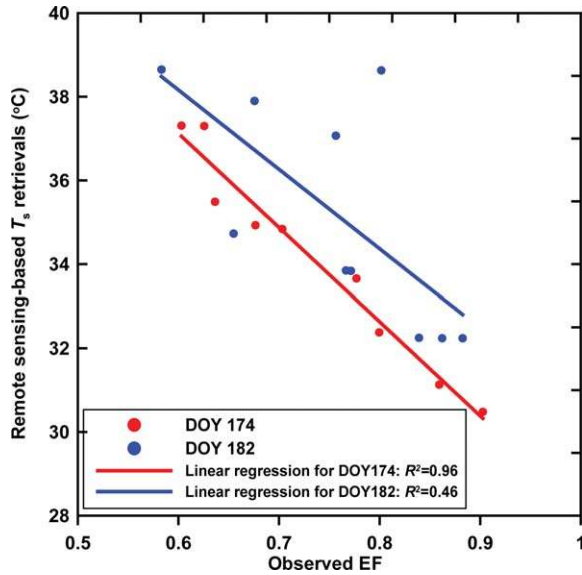
Figure 6. Regression analysis of ground-based EF measurements and corresponding remote sensing-based T_s retrievals for DOY 174 and DOY 182.

progressively increasing spatial mean for cases 1–3, cases 4–6, and cases 7–9, respectively. This finding is consistent with the performance of the three spatial variability models at EC tower scales discussed in section 5.1. Differing end-members for the same model can result in different spatial means of the EF estimates.

[34] Second, varying end-members for these models does not substantially influence the standard deviation and skewness of the EF estimates. The shape of the frequency distribution for the same model remains essentially invariant under the changing end-members. Only the positions of these frequency distributions relative to the origin are different. This is because varying the end-members of a model does not alter its model physics, and consequently, cannot affect the pattern of output. A reasonable magnitude of spatial mean of EF from a model can therefore be derived by properly tuning the magnitude of T_{max} and/or T_{min} if the detailed and accurate spatial distribution of EF or LE is not the primary issue of concern. This finding would be meaningful to coarse-spatial-resolution images of operational satellites (e.g., Terra/Aqua-MODIS and GOES) as they are often utilized to generate large-scale EF or ET_a, instead of capturing EF or ET_a at field scales. This is because tuning end-members from coarse-spatial-resolution images makes it possible to generate reasonable magnitudes of regional EF or ET_a estimates.

[35] Third, different models show markedly different shapes of the frequency distributions of EF estimates (Figures 7 and 8 and Figures S1–S4). SEBAL and METRIC generated a similar frequency distribution of EF estimates for nine cases on both days, with the skewness $\sim$0.185 on DOY 174, and $\sim$0.435 on DOY 182. The EF frequency distributions from the triangle model are different, showing the skewness of 0.01 and -0.17 on DOY 174 and DOY 182, respectively. Differences in the skewness between the triangle and SEBAL-type models are due to different model physics and definitions of limiting edges of EF within the f_c-T_s space.

[36] Fourth, the EF frequency distributions from the three models generally exhibit a bimodal separation of flux patterns from corn and soybean fields on DOY 174 (Figures 7 and 8, and Figure S1) and DOY 182 (Figures S2–S4), in which DOY 182 showed a more pronounced bimodal separation. This is because under rapid growth in corn and soybean, differences in heat and water fluxes between the two crops would be more marked on the latter day. Utility of these models to capture spatial differences in water and heat fluxes can be ascribed mostly to the ability of thermal infrared remote sensor data to respond to the reality of the specific time-of-day energy balance partitioning.

5.3. Explicit Expression of Limiting Edges of EF for Triangle and SEBAL-Type Models

[37] Coefficients a and b in equation (17) were derived from the combinations of extremes, which resulted in the highest EF accuracy shown in section 5.1 (referring to Table 4), i.e., case 9 for DOY 174 and case 1 for DOY 182. Numerical solutions of T'_{max} in equation (17) are shown in Figure 9.

[38] As illustrated in section 4.2, temperatures of $EF = 0$ and $EF \approx 1$ ($\phi_{max} \cdot \Delta/(\Delta + \gamma) = 0.99$ at $T_a = 29.6°C$ for DOY 174 and $= 0.988$ at $T_a = 29.4°C$ for DOY 182) for the triangle model form two horizontal limiting edges, i.e., T_{max} and T_{min}, throughout the f_c-T_s space (Figure 9). Temperature of surfaces where $EF = 1$ for SEBAL is T_{min}. It is interesting to note that temperature of surfaces where $EF = 0$ for SEBAL is curvilinear, and increases with increasing f_c, which seems to contradict a realistic decreasing warm edge with increasing f_c [*Moran et al.*, 1994]. The increasing limiting edge of $EF = 0$ intrinsic in SEBAL is primarily because $A_i(T_a)$ tends to increase with increasing f_c, and constants a and b do not account for the effect of variation in f_c on the limiting edge of $EF = 0$.

6. Discussion

[39] There are three key issues regarding the applicability of spatial variability models: (1) how the end-members determine the magnitudes and distributions of EF or LE estimates; (2) whether the end-members can be appropriately selected or determined by the operator or by other automatic methods; and (3) whether the limiting edges of EF within the f_c-T_s space can represent the reality for a study site of interest.

6.1. How the End-Members Determine the Magnitudes and Distributions of EF Estimates

[40] To quantify the impact of end-members on EF or LE estimates from spatial variability models, some studies have performed sensitivity analyses and evaluated their accuracy with a relatively dense network of EC or EBBR towers under a certain climate and environmental condition. Note that taking only one pair of end-members from a specific scene of image may not gain a full understanding of how variation in end-members impacts the magnitude, distribution, and accuracy of a model. *Timmermans et al.* [2007] performed a sensitivity analysis of SEBAL by tuning T_{max} and T_{min} with ± 2 K, and found variations in the H estimates on the order of 20–25%. *Long et al.* [2011] assessed the sensitivity of SEBAL by using 29 MODIS scenes acquired across varying meteorological conditions
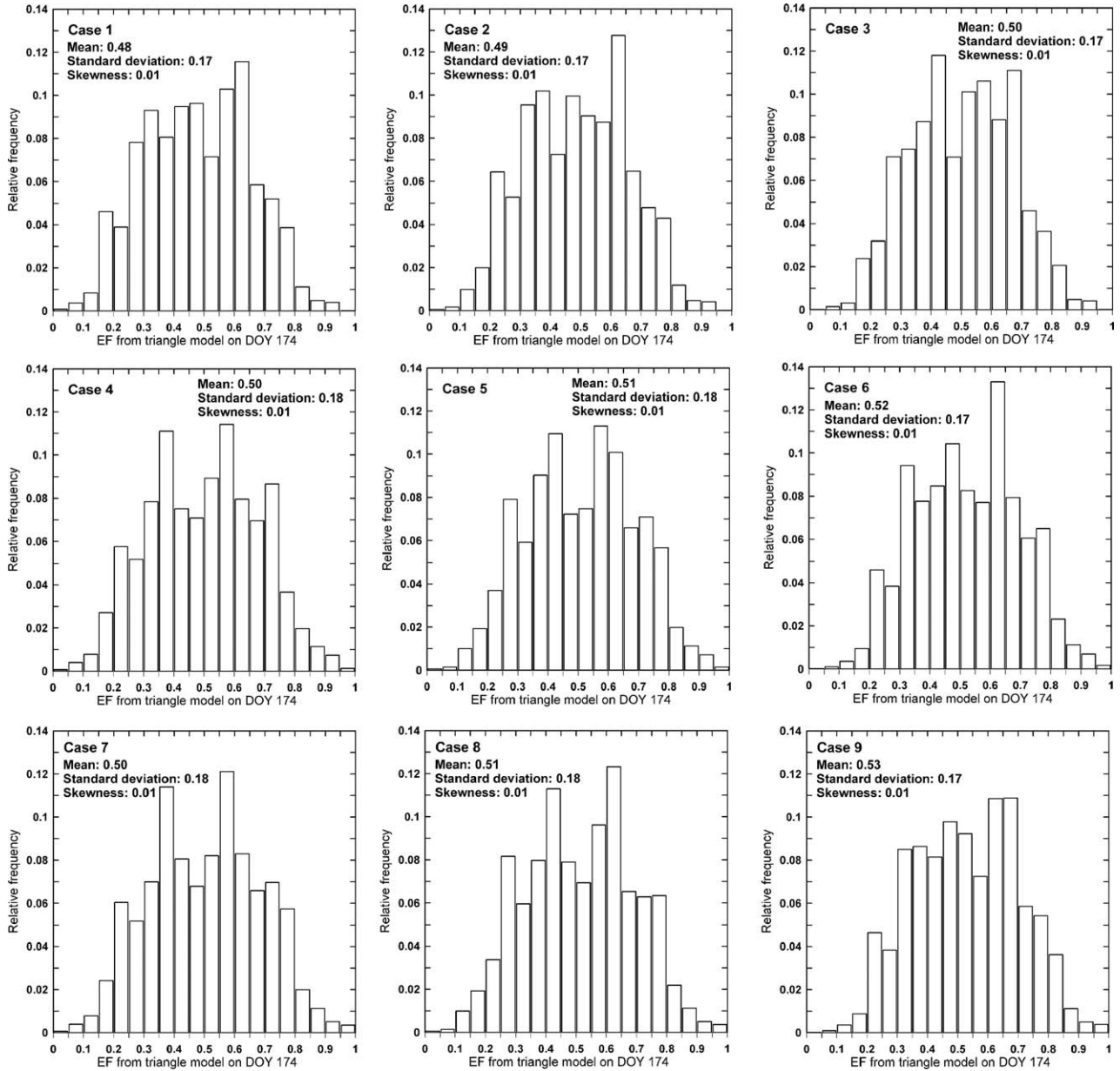
Figure 7. Frequency distributions of EF estimates from the triangle model on DOY 174 for nine combinations of extremes corresponding to cases 1–9 in Table 3, showing statistics of spatial mean, standard deviation, and skewness for each case.

and diverse landscapes, indicating that variations of ± 2 K in $T_{max}(T_{min})$ can result in variations in the H estimates on the order of 10–15%, and variations in ± 5 K in $T_{max}(T_{min})$ can result in variations in the H estimates on the order of 25–50%. Both hot and cold pixels in SEBAL have a similar effect on the magnitudes of variation in H and therefore LE estimates [*Long et al.*, 2011; *Timmermans et al.*, 2007]. Results of this study at both field tower scale and watershed scales demonstrate that varying magnitudes of T_{max} or T_{min} can result in a shift in the mean, but cannot greatly alter the shape of the EF frequency distribution, evidenced by generally similar standard deviation and skewness. The frequency distribution of EF is closely related to that of T_s, which is demonstrated across all EC towers in section 5.1 and by some other studies [e.g., *Choi et al.*, 2009; *Gao and*

Long, 2008]. It can therefore be generalized that for all spatial variability models, elevating T_{max} or T_{min} can lead to increases in the resulting EF or LE estimates. On the contrary, damping T_{max} or T_{min} can result in decreases in EF or LE estimates. This finding would be useful for calibration of the spatial variability models because systematic biases of some spatial variability models could be removed or reduced by modifying the magnitudes of T_{max} or T_{min}, or other associated characteristic variables, e.g., A_{hot}, which is analogous to elevating or damping T_{max} or T_{min}. It is important to note that tuning characteristic variables of end-members or end-member selection themselves could reconcile the discrepancies between estimates and measurements for pixels with moderate T_s values in some cases; distortion of the flux estimates could, however, occur over relatively dry
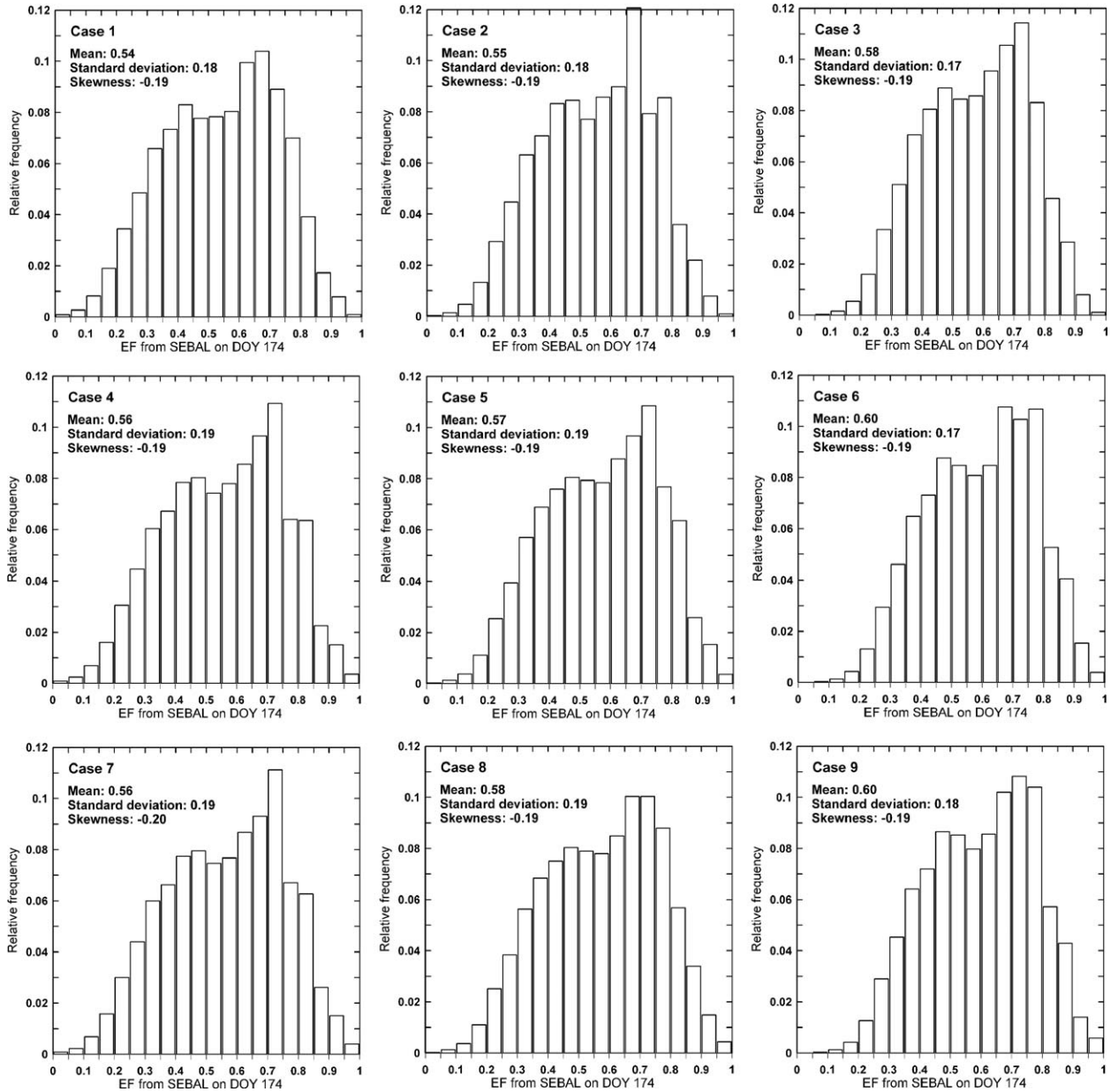
Figure 8. Frequency distributions of EF estimates from the SEBAL model on DOY 174 for nine combinations of extremes corresponding to cases 1–9 in Table 3, showing statistics of spatial mean, standard deviation, and skewness for each case.

or wet surfaces. For instance, increasing T_{max} but meanwhile decreasing T_{min} may not result in appreciable differences in EF estimates for surfaces with moderate T_s values; the two effects offset each other. However, erroneous EF estimates for pixels close to the upper and lower limiting edges would occur.

6.2. Whether the End-Members Can Be Appropriately Selected or Determined

[41] Selection of end-members is another critical issue that has been controversial in the remote sensing-based ET estimation community. The model developers claimed difficulties and subjectivity in selecting end-members [e.g., *Allen et al.*, 2007; *Bastiaanssen et al.*, 2010], and other researchers have confirmed this through a number of theo-

retical and experimental studies [e.g., *Choi et al.*, 2009; *French et al.*, 2005a, 2005b; *Long and Singh*, 2012b; *McVicar and Jupp*, 1998; *Timmermans et al.*, 2007]. This is because different extents of study sites and spatial resolutions of satellite images could have variable contrast in soil moisture and f_c, which may fundamentally determine the magnitudes of T_{max} and T_{min} and therefore result in differing EF and LE retrievals. For instance, selection of the hot extreme from a humid agricultural field (e.g., the SMA-CEX) could be problematic, and the cold extreme may not exist over arid and semiarid regions. Moreover, seasonal variation in vegetation and crops could also result in different contrasts in soil moisture and f_c. Satellite images acquired in late autumn, winter, and early spring could exhibit more homogeneous wetness and surface cover

Table 5. Statistics of Frequency Distributions of EF Estimates From Triangle, SEBAL, and METRIC Models for Nine Combinations of Selected Extremes on DOY 174 and DOY 182[a]

| Model	Cold Pixel	Hot Pixel	DOY 174 μ	DOY 174 σ	DOY 174 γ	DOY 182 μ	DOY 182 σ	DOY 182 γ
Triangle	1	1	*0.48*	*0.17*	*0.01*	*0.59*	*0.16*	*−0.17*
		2	0.49	0.17	0.01	0.61	0.16	−0.17
		3	0.50	0.17	0.01	0.64	0.14	−0.17
	2	1	0.50	0.18	0.01	0.60	0.16	−0.17
		2	0.51	0.18	0.01	0.62	0.16	−0.17
		3	0.52	0.17	0.01	0.65	0.14	−0.17
	3	1	0.50	0.18	0.01	0.65	0.18	−0.17
		2	0.51	0.18	0.01	0.67	0.17	−0.17
		3	*0.53*	*0.17*	*0.01*	0.69	0.15	−0.17
SEBAL	1	1	*0.54*	*0.18*	*−0.19*	*0.67*	*0.16*	*−0.43*
		2	0.55	0.18	−0.19	0.69	0.16	−0.43
		3	0.58	0.17	−0.19	0.71	0.14	−0.43
	2	1	0.56	0.19	−0.19	0.67	0.17	−0.43
		2	0.57	0.19	−0.19	0.69	0.16	−0.43
		3	0.60	0.17	−0.19	0.72	0.14	−0.43
	3	1	0.56	0.19	−0.20	0.72	0.17	−0.44
		2	0.58	0.19	−0.19	0.73	0.16	−0.44
		3	*0.60*	*0.18*	*−0.19*	*0.75*	*0.15*	*−0.43*
METRIC	1	1	*0.60*	*0.15*	*−0.18*	*0.71*	*0.14*	*−0.43*
		2	0.61	0.15	−0.18	0.72	0.13	−0.43
		3	0.62	0.14	−0.18	0.74	0.12	−0.42
	2	1	0.61	0.16	−0.19	0.71	0.14	−0.43
		2	0.62	0.15	−0.18	0.73	0.13	−0.43
		3	0.64	0.15	−0.18	0.75	0.12	−0.42
	3	1	0.62	0.16	−0.18	0.74	0.15	−0.43
		2	0.63	0.15	−0.19	0.76	0.14	−0.43
		3	*0.65*	*0.15*	*−0.19*	*0.78*	*0.13*	*−0.43*

[a]Cold extremes 1–3 and hot extremes 1–3 are in increasing order of the magnitude of temperature (referring to Figure 3), respectively. Greek letters μ, σ, and γ denote the mean, standard deviation, and skewness of the EF estimates. The values in italics show extreme statistics of each model for the nine cases on each day.

conditions, which may result in underperformance of spatial variability models. Therefore, determination of end-members and applicability of spatial variability models may also depend on the season. Furthermore, evaluation of SEBAL and METRIC herein has shown that during rapid growth in crops in rainfed fields coinciding with marked variation in soil moisture, locations of end-members may vary with days. This may not hold true over irrigated areas where the cold extreme may be fixed to certain surfaces if contamination by clouds can be favorably removed from a scene [*Allen et al.*, 2007; *Long et al.*, 2011]. In practice, varying extents and spatial resolutions of satellite images would be available, and it is not occasional to obtain images contaminated by clouds. These issues exacerbate difficulties and uncertainties in selecting end-members [*Marx et al.*, 2008; *Verstraeten et al.*, 2005]. It is noted that METRIC tends to do better at the cold extreme by using ground-based reference ET to resolve the energy balance for the cold end. However, the determination of actual ET for the hot extreme appears to be more difficult and sometimes needs consultation with the model developers [e.g., *Choi et al.*, 2009].

[42] Limiting edges for triangle models can also be derived by regression analysis of f_c-T_s or α-T_s scatterplots [e.g., *Jiang and Islam*, 2001; *Verstraeten et al.*, 2005]. To apply the triangle model to arid areas where the lower limiting edge of EF appears to rarely exist in a scene, the upper limiting edge was extended to intersect with $f_c = 1$ to infer a constant lower limiting edge [*Tang et al.*, 2010]. However, this method still overestimates the lower limiting edge, evidenced by pixels with relatively high f_c and lower T_s than the inferred lower limiting edge [see *Tang et al.*, 2010, Figure 7]. Derivation of limiting edges appears to be far less than satisfactory, and determination of end-members for spatial variability models has not been fully resolved.

[43] On the other hand, TSEB and SEBS tend to be context independent, not being affected by uncertainties in the selection of end-members [e.g., *French et al.*, 2003; *Kalma et al.*, 2008]. This is achieved by (1) a more realistic description of the two-source scheme involved in TSEB [*Kustas and Anderson*, 2009; *Kustas et al.*, 2007] or (2) increasing the input effort of meteorological variables (e.g., T_a and e_a) to derive wet and dry limits for each pixel for SEBS [*Su*, 2002]. Some approaches do not necessitate end-member selection, either, e.g., the normalized difference temperature index (NDTI) [*McVicar and Jupp*, 1998, 1999, 2002], the two-source trapezoid model for ET (TTME) [*Long and Singh*, 2012a], and a modified TTME model [*Yang and Shang*, 2013]. Critical in TSEB and SEBS is the use of the Priestley-Taylor equation to determine the wet limit of transpiration from vegetation canopy for TSEB and the use of relatively coarse meteorological fields to determine the wet and dry limits of LE based on the Penman-Monteith equation for each pixel for SEBS. These issues combined with associated procedures were investigated [e.g., *Agam et al.*, 2010] and warrant further study. To fully understand longer-term evaporative dynamics, including the recently widely reported declines in observed atmospheric evaporative ability made by measuring pan evaporation [*McVicar et al.*, 2012], fully physically based estimates of potential ET are advocated.
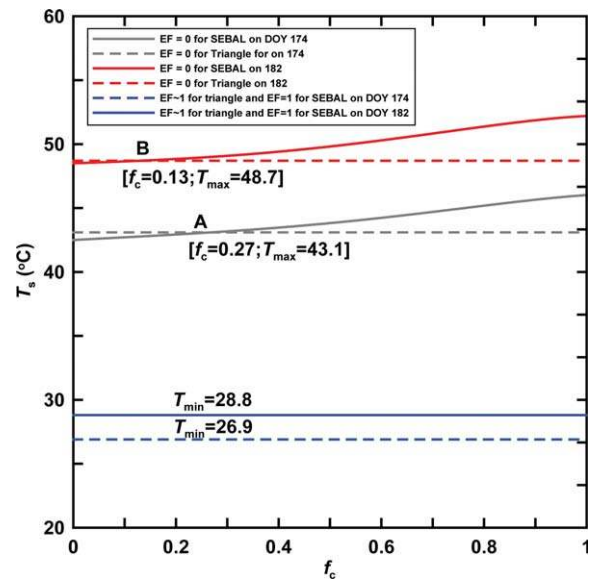
Figure 9. Temperatures of limiting edges of EF = 1(or ≈1) and EF = 0 intrinsic in the triangle and SEBAL models for a full range of f_c on DOY 174 and DOY 182, respectively. Letters A and B represent hot extremes on the 2 days.

6.3. Whether the Limiting Edges of EF Within the f_c-T_s Space Can Represent the Reality for a Study Site of Interest

[44] Notable differences in the frequency distributions of EF estimates between triangle and SEBAL-type models were observed. Distinct patterns between the one-source models and the two-source models have also been found [e.g., *Choi et al.*, 2009; *French et al.*, 2005a; *Gao and Long*, 2008; *McCabe and Wood*, 2006; *Timmermans et al.*, 2007], though they were able to generate comparable estimates of LE or ET_a at field scales. We conclude that the end-members are one of the primary reasons responsible for the different frequency distributions. Analyses in sections 4.2 and 5.3 demonstrate that the upper limiting edges of EF between the triangle model and the SEBAL-type model are different, with the limiting edges of the triangle model being explicitly shown and remaining constant across the f_c-T_s space, and the upper limiting edge of the SEBAL-type models being implicitly shown and increasing as f_c increases. These limiting edges can only be taken as a rough approximation of reality. Different wet and dry limits for each f_c class for different models can result in different magnitudes of EF estimates and consequently the varying frequency distributions over the modeling domain.

[45] *Timmermans et al.* [2007] indicated that tuning T_{max} or T_{min} for a specific land cover could minimize the discrepancies between H estimates and ground-based measurements, which, however, was compromised by degrading H estimates for other land cover types. This finding can be further explained by the study herein. For instance, tuning T_{max} so as to make the upper limiting edge of the SEBAL-type models for low f_c surfaces closer to the theoretical limiting edges depicted by a trapezoid space [*Long and Singh*, 2012a; *Moran et al.*, 1994] (referring to trapezoid ABCD in Figure 1), it is likely to increase the discrepancies over high f_c surfaces. This may also explain the reason why tuning the ET_rF for the bare surface in METRIC can lead to improvements in the LE estimates for a certain crop but degrade the estimates for the other [*Choi et al.*, 2009].

[46] The critical studies mentioned earlier suggest that determination of end-members of spatial variability models tends to be far less than satisfactory, depending largely on subjectivity, spatial extent, and/or resolution of satellite images. As output of these spatial variability models is not deterministic in most cases, utility and robustness of these models are severely impaired. Efforts have been made to more realistically depict the limiting edges of spatial variability models. Based on field experiments and theoretical analysis, *Moran et al.* [1994] developed a trapezoid framework for the vegetation index-T_s space to configure the limiting edges of crop water deficit, with the hot edge decreasing with increasing vegetation index. *McVicar and Jupp* [1998] developed the NDTI approach, which calculates extreme temperatures at meteorological stations by inverting a specific-time-of-day resistance energy balance model (REBM). We suggest that derivation of end-members based on *Moran et al.* [1994]'s framework would be an effective way to amend the limiting edges of spatial variability models, and therefore provide more reliable spatial patterns of EF or LE estimates.

7. Conclusion

[47] We examined the impact of end-member selection on the performance and mechanisms of error propagation of three satellite-based spatial variability models for ET_a estimation, i.e., the triangle model, SEBAL, and METRIC. Varying end-members can result in markedly different magnitudes of EF estimates at both field and watershed scales. The hot and cold extremes exercise a similar impact on the discrepancy between EF estimates and ground-based measurements, i.e., given a hot (cold) extreme, the EF estimates tend to increase with increasing cold (hot) extreme, and decrease with decreasing cold (hot) extreme. Predictability of all spatial variability models depends primarily on the capability of T_s to capture EF and definitions of limiting edges of EF within the remotely sensed f_c-T_s space. In most cases, the end-members cannot be appropriately determined from the f_c-T_s space, because (1) they do not necessarily exist within a scene, varying with the spatial extent and resolution of satellite images being used; and/or (2) different operators can select different end-members. In addition, the limiting edge of EF $= 0$ in the f_c-T_s space varies with the model, with SEBAL-type models showing an increasing curvilinear edge, which contradicts a decreasing edge shown in a trapezoidal framework [*Moran et al.*, 1994]. Varying end-members cannot substantially affect the standard deviation and skewness of the EF frequency distribution. However, different models can generate remarkably different EF frequency distributions due to differing limiting edges. As such, the spatial variability models require careful calibration to infer reasonable EF limits and then LE and ET_a estimates. In water resources management, these spatial variability models should be used with great caution, because ET_a estimates can be significantly different due to slight differences in selected end-members.

References

Agam, N., W. P. Kustas, M. C. Anderson, J. M. Norman, P. D. Colaizzi, T. A. Howell, J. H. Prueger, T. D. Meyers, and T. B. Wilson (2010), Application of the Priestley-Taylor approach in a two-source surface energy balance model, *J. Hydrometeorol.*, *11*(1), 185–198.

Allen, R. G., L. S. Pereira, D. Raes, and M. Smith (1998), Crop evapotranspiration-Guidelines for computing crop water requirements. *FAO Irrig. and Drainage Pap. 56*. United Nations Food and Agric. Organ., Rome.

Allen, R. G., M. Tasumi, and R. Trezza (2007), Satellite-based energy balance for mapping evapotranspiration with internalized calibration (METRIC)—Model, *J. Irrig. Drain. Eng.*, *133*(4), 380–394.

Anderson, M. C., J. M. Norman, W. P. Kustas, F. Li, J. H. Prueger, and J. R. Mecikalski (2005), Effects of vegetation clumping on two-source model estimates of surface energy fluxes from an agricultural landscape during SMACEX, *J. Hydrometeorol.*, *6*(6), 892–909.

Anderson, M. C., J. M. Norman, J. R. Mecikalski, J. A. Otkin, and W. P. Kustas (2007), A climatological study of evapotranspiration and moisture stress across the continental United States based on thermal remote sensing: 1. Model formulation, *J. Geophys. Res.*, *112*, D10117, doi:10.1002/2006JD007506.

Bastiaanssen, W. G. M. (2000), SEBAL-based sensible and latent heat fluxes in the irrigated Gediz Basin, Turkey, *J. Hydrol.*, *229*(1-2), 87–100.

Bastiaanssen, W. G. M., M. Menenti, R. A. Feddes, and A. A. M. Holtslag (1998), A remote sensing surface energy balance algorithm for land (SEBAL). 1. Formulation, *J. Hydrol.*, *213*(1-4), 198–212.

Bastiaanssen, W. G. M., M.-D. Ahmad, and Y. Chemin (2002), Satellite surveillance of evaporative depletion across the Indus Basin, *Water Resour. Res.*, *38*(12), 1273, doi:10.1002/2001WR000386.

Bastiaanssen, W. G. M., E. J. M. Noordman, H. Pelgrum, G. Davids, B. P. Thoreson, and R. G. Allen (2005), SEBAL model with remotely sensed data to improve water-resources management under actual field conditions, *J. Irrig. Drain. Eng.*, *131*(1), 85–93.

Bastiaanssen, W., B. Thoreson, B. Clark, and G. Davids (2010), Discussion of ''Application of SEBAL model for mapping evapotranspiration and estimating surface energy fluxes in South-Central Nebraska'' by Ramesh K. Singh, Ayse Irmak, Suat Irmak, and Derrel L. Martin, *J. Irrig. Drain. Eng.*, *136*(4), 282–283.

Batra, N., S. Islam, V. Venturini, G. Bisht, and J. Jiang (2006), Estimation and comparison of evapotranspiration from MODIS and AVHRR sensors for clear sky days over the Southern Great Plains, *Remote Sens. Environ.*, *103*(1), 1–15.

Carlson, T. (2007), An overview of the ''triangle method'' for estimating surface evapotranspiration and soil moisture from satellite imagery, *Sensors*, *7*(8), 1612–1629.

Carlson, T. N., W. J. Capehart, and R. R. Gillie (1995a), A new look at the simplified method for remote-sensing of daily evapotranspiration, *Remote Sens. Environ.*, *54*(2), 161–167.

Carlson, T. N., R. R. Gillies, and T. J. Schmugge (1995b), An interpretation of methodologies for indirect measurement of soil-water content, *Agric. For. Meteorol.*, *77*(3-4), 191–205.

Carlson, T. N., O. Taconet, A. Vidal, R. R. Gilles, A. Olioso, and K. Humes (1995c), An overview of the workshop on thermal remote-sensing held at La-Londe-les-Maures, France, September 20–24, 1993, *Agric. For. Meteorol.*, *77*(3-4), 141–151.

Choi, M., W. P. Kustas, M. C. Anderson, R. G. Allen, F. Q. Li, and J. H. Kjaersgaard (2009), An intercomparison of three remote sensing-based surface energy balance algorithms over a corn and soybean production region (Iowa, US) during SMACEX, *Agric. For. Meteorol.*, *149*(12), 2082–2097.

French, A. N., T. J. Schmugge, W. P. Kustas, K. L. Brubaker, and J. Prueger (2003), Surface energy fluxes over El Reno, Oklahoma, using high-resolution remotely sensed data, *Water Resour. Res.*, *39*(6), doi:10.1002/2002WR001734.

French, A. N., et al. (2005a), Surface energy fluxes with the Advanced Spaceborne Thermal Emission and Reflection radiometer (ASTER) at the Iowa 2002 SMACEX site (USA), *Remote Sens. Environ.*, *99*(1-2), 55–65.

French, A. N., et al. (2005b), Corrigendum to ''Surface energy fluxes with the Advanced Spaceborne Thermal Emission and Reflection radiometer (ASTER) at the Iowa 2002 SMACEX site (USA) (vol 99, pg 55, 2005)'', *Remote Sens. Environ.*, *99*(4), 471–471.

Gao, Y. C., and D. Long (2008), Intercomparison of remote sensing-based models for estimation of evapotranspiration and accuracy assessment based on SWAT, *Hydrol. Process.*, *22*(25), 4850–4869.

Gillies, R. R., T. N. Carlson, J. Cui, W. P. Kustas, and K. S. Humes (1997), A verification of the 'triangle' method for obtaining surface soil water content and energy fluxes from remote measurements of the Normalized Difference Vegetation Index (NDVI) and surface radiant temperature, *Int. J. Remote Sens.*, *18*(15), 3145–3166.

Gonzalez-Dugo, M. P., C. M. U. Neale, L. Mateos, W. P. Kustas, J. H. Prueger, M. C. Anderson, and F. Li (2009), A comparison of operational remote sensing-based models for estimating crop evapotranspiration, *Agric. For. Meteorol.*, *149*(11), 1843–1853.

Jiang, L., and S. Islam (2001), Estimation of surface evaporation map over southern Great Plains using remote sensing data, *Water Resour. Res.*, *37*(2), 329–340.

Jiang, L., S. Islam, W. Guo, A. S. Jutla, S. U. S. Senarath, B. H. Ramsay, and E. A. B. Eltahir (2009), A satellite-based daily actual evapotranspiration estimation algorithm over South Florida, *Global Planet. Change*, *67*(1-2), 62–77.

Kalma, J. D., T. R. McVicar, and M. F. McCabe (2008), Estimating land surface evaporation: A review of methods using remotely sensed surface temperature data, *Surv. Geophys.*, *29*(4-5), 421–469.

Kustas, W., and M. Anderson (2009), Advances in thermal infrared remote sensing for land surface modeling, *Agric. For. Meteorol.*, *149*(12), 2071–2081.

Kustas, W. P., J. L. Hatfield, and J. H. Prueger (2005), The soil moisture-atmosphere coupling experiment (SMACEX): Background, hydrometeorological conditions, and preliminary findings, *J. Hydrometeorol.*, *6*(6), 791–804.

Kustas, W. P., M. C. Anderson, J. M. Norman, and F. Q. Li (2007), Utility of radiometric-aerodynamic temperature relations for heat flux estimation, *Bound.-Layer Meteorol.*, *122*(1), 167–187.

Li, F. Q., T. J. Jackson, W. P. Kustas, T. J. Schmugge, A. N. French, M. H. Cosh, and R. Bindlish (2004), Deriving land surface temperature from Landsat 5 and 7 during SMEX02/SMACEX, *Remote Sens. Environ.*, *92*(4), 521–534.

Li, F. Q., W. P. Kustas, M. C. Anderson, J. H. Prueger, and R. L. Scott (2008), Effect of remote sensing spatial resolution on interpreting tower-based flux observations, *Remote Sens. Environ.*, *112*(2), 337–349.

Long, D., and V. P. Singh (2010), Integration of the GG model with SEBAL to produce time series of evapotranspiration of high spatial resolution at watershed scales, *J. Geophys. Res.*, *115*, D21128, doi:10.1002/2010JD014092.

Long, D., Y. C. Gao, and V. P. Singh (2010), Estimation of daily average net radiation from MODIS data and DEM over the Baiyangdian watershed in North China for clear sky days, *J. Hydrol.*, *388*(3-4), 217–233.

Long, D., V. P. Singh, and Z.-L. Li (2011), How sensitive is SEBAL to changes in input variables, domain size and satellite sensor?, *J. Geophys. Res.*, *116*, doi:10.1029/2011JD016542.

Long, D., and V. P. Singh (2012a), A two-source trapezoid model for evapotranspiration (TTME) from satellite imagery, *Remote Sens. Environ.*, *121*, 370–388.

Long, D., and V. P. Singh (2012b), A modified surface energy balance algorithm for land (M-SEBAL) based on a trapezoidal framework, *Water Resour. Res.*, *48*, W02528, doi:10.1029/2011WR010607.

Mackay, D. S., B. E. Ewers, B. D. Cook, and K. J. Davis (2007), Environmental drivers of evapotranspiration in a shrub wetland and an upland forest in northern Wisconsin, *Water Resour. Res.*, *43*, W03442, doi:10.1029/2006WR005149.

Marx, A., H. Kunstmann, D. Schuttemeyer, and A. F. Moene (2008), Uncertainty analysis for satellite derived sensible heat fluxes and scintillometer measurements over Savannah environment and comparison to mesoscale meteorological simulation results, *Agric. For. Meteorol.*, *148*(4), 656–667.

McCabe, M. F., and E. F. Wood (2006), Scale influences on the remote estimation of evapotranspiration using multiple satellite sensors, *Remote Sens. Environ.*, *105*(4), 271–285.

McVicar, T. R., and D. L. B. Jupp (1998), The current and potential operational uses of remote sensing to aid decisions on drought exceptional circumstances in Australia: A review, *Agric. Syst.*, *57*(3), 399–468.

McVicar, T. R., and D. L. B. Jupp (1999), Estimating one-time-of-day meteorological data from standard daily data as inputs to thermal remote sensing based energy balance models, *Agric. For. Meteorol.*, *96*(4), 219–238.

McVicar, T. R., and D. L. B. Jupp (2002), Using covariates to spatially interpolate moisture availability in the Murray-Darling Basin—A novel use of remotely sensed data, *Remote Sens. Environ.*, *79*(2-3), 199–212.

McVicar, T. R., et al. (2012), Global review and synthesis of trends in observed terrestrial near-surface wind speeds: Implications for evaporation, *J. Hydrol.*, *416*, 182–205.

Moran, M. S., T. R. Clarke, Y. Inoue, and A. Vidal (1994), Estimating crop water-deficit using the relation between surface-air temperature and spectral vegetation index, *Remote Sens. Environ.*, *49*(3), 246–263.

Norman, J. M., W. P. Kustas, and K. S. Humes (1995), A two-source approach for estimating soil and vegetation energy fluxes in observations of directional radiometric surface-temperature, *Agric. For. Meteorol.*, *77*(3-4), 263–293.

Norman, J. M., M. C. Anderson, W. P. Kustas, A. N. French, J. Mecikalski, R. Torn, G. R. Diak, T. J. Schmugge, and B. C. W. Tanner (2003), Remote sensing of surface energy fluxes at 10(1)-m pixel resolutions, *Water Resour. Res.*, *39*(8), 1221, doi:10.1029/2002WR001775.

Price, J. C. (1990), Using spatial context in satellite data to infer regional scale evapotranspiration, *IEEE Trans. Geosci. Remote Sens.*, *28*(5), 940–948.

Prueger, J. H., J. L. Hatfield, W. P. Kustas, L. E. Hipps, J. I. MacPherson, C. M. U. Neale, W. E. Eichinger, D. I. Cooper, and T. B. Parkin (2005), Tower and aircraft eddy covariance measurements of water vapor, energy, and carbon dioxide fluxes during SMACEX, *J. Hydrometeorol.*, *6*(6), 954–960.

Roerink, G. J., Z. Su, and M. Menenti (2000), S-SEBI: A simple remote sensing algorithm to estimate the surface energy balance, *Phys. Chem. Earth B*, *25*(2), 147–157.

Sandholt, I., K. Rasmussen, and J. Andersen (2002), A simple interpretation of the surface temperature/vegetation index space for assessment of surface moisture status, *Remote Sens. Environ.*, *79*(2-3), 213–224.

Schellekens, J., F. N. Scatena, L. A. Bruijnzeel, and A. J. Wickel (1999), Modelling rainfall interception by a lowland tropical rain forest in northeastern Puerto Rico, *J. Hydrol.*, *225*(3-4), 168–184.

Su, Z. (2002), The Surface Energy Balance System (SEBS) for estimation of turbulent heat fluxes, *Hydrol. Earth Syst. Sci.*, *6*(1), 85–99.

Tang, R. L., Z. L. Li, and B. H. Tang (2010), An application of the Ts-VI triangle method with enhanced edges determination for evapotranspiration estimation from MODIS data in and and semi-arid regions: Implementation and validation, *Remote Sens. Environ.*, *114*(3), 540–551.

Tasumi, M. (2003), Progress in operational estimation of regional evapotranspiration using satellite imagery, Ph.D. dissertation. Dept. Biological and Agricultural Engineering, University of Idaho, Moscow, Idaho, 357 p.

Timmermans, W. J., W. P. Kustas, M. C. Anderson, and A. N. French (2007), An intercomparison of the surface energy balance algorithm for land (SEBAL) and the two-source energy balance (TSEB) modeling schemes, *Remote Sens. Environ.*, *108*(4), 369–384.

Van Niel, T. G., T. R. McVicar, M. L. Roderick, A. I. J. M. van Dijk, L. J. Renzullo, and E. van Gorsel (2011), Correcting for systematic error in satellite-derived latent heat flux due to assumptions in temporal scaling: Assessment from flux tower observations, *J. Hydrol.*, *409*(1–2), 140–148.

Verstraeten, W. W., F. Veroustraete, and J. Feyen (2005), Estimating evapotranspiration of European forests from NOAA-imagery at satellite overpass time: Towards an operational processing chain for integrated optical and thermal sensor data products, *Remote Sens. Environ.*, *96*(2), 256–276.

Verstraeten, W. W., F. Veroustraete, and J. Feyen (2008), Assessment of evapotranspiration and soil moisture content across different scales of observation, *Sensors*, *8*(1), 70–117.

Wang, J., T. W. Sammis, V. P. Gutschick, M. Gebremichael, and D. R. Miller (2009), Sensitivity analysis of the surface energy balance algorithm for land (SEBAL), *T ASABE*, *52*(3), 801–811.

Yang, Y., and S. Shang (2013), A hybrid dual source scheme and trapezoid framework based evapotranspiration model (HTEM) using satellite images: Algorithm and model test, *J. Geophys. Res.*, *118*, doi:10.1002/jgrd.50259.